energies

Article

Design and Analysis of a 30 kW, 30,000 r/min High-Speed Permanent Magnet Motor for Compressor Application

Zhenning Qi [1], Yue Zhang [1,*], Siyang Yu [2] and Zhenyao Xu [2]

[1] School of Electrical Engineering, Shandong University, Jinan 250061, China; zhenningqi@163.com
[2] School of Electrical Engineering, Shenyang University of Technology, Shenyang 110870, China; yusy@sut.edu.cn (S.Y.); xuzy@sut.edu.cn (Z.X.)
* Correspondence: yzhang35@sdu.edu.cn

Abstract: In this paper, the design and analysis of a 30 kW, 30,000 r/min high-speed permanent magnet motor (HSPMM) for compressor application are provided. In order to provide a reasonable electromagnetic design scheme, the electromagnetic performances of the HSPMM under different structures are analyzed and compared by the finite element method (FEM). The thermal performances and cooling system of the HSPMM are, respectively, analyzed and designed by computational fluid dynamics (CFD). Finally, the HSPMM's rotor strength is studied by both FEM and analytical methods, and the influencing factors of which are also researched in this paper.

Keywords: high-speed permanent magnet motor; FEM; electromagnetic design; CFD; thermal analysis; analytical method; rotor strength

Citation: Qi, Z.; Zhang, Y.; Yu, S.; Xu, Z. Design and Analysis of a 30 kW, 30,000 r/min High-Speed Permanent Magnet Motor for Compressor Application. *Energies* **2022**, *15*, 3923. https://doi.org/10.3390/en15113923

Academic Editor: Anna Richelli

Received: 20 April 2022
Accepted: 21 May 2022
Published: 26 May 2022

1. Introduction

High-speed permanent magnet motors (HSPMMs) have the advantages of compact structure, high power density, and high efficiency [1–3]. Compared with the traditional method of driving high-speed loads by using a constant speed motor and gearbox, it is more effective to reduce the volume of the driving system, increase power density and improve operation efficiency by using HSPMM directly, so that HSPMM has a promising future and a wide range of applications such as high-speed compressors, flywheel energy storage, and so on. However, the performances of HSPMM in multiple physical fields also need to be further investigated because of their high frequency, high speed, and high loss density [4]. Therefore, a 30 kW, 30,000 r/min HSPMM for compressor application is designed and analyzed in multi-physics fields in this paper.

Firstly, this paper provides analyses of the influencing factors of the HSPMM's electromagnetic performances such as the motor main dimensions, the number of poles, the number of stator slots, and the magnetization method of PM.

Due to the high power density and compact size, the heat dissipation capacity of HSPMM is limited, which may result in the demagnetization of PM. Therefore, the thermal analysis and cooling system design of the HSPMM are particularly necessary.

Considering the PM materials are fragile in tensile, it is necessary to install a sleeve outside the rotor for mechanical protection. This paper analyzes the rotor stress distribution of the HSPMM by both analytical and FEM methods. The influencing factors such as sleeve thickness and interference are also analyzed in this paper.

2. Electromagnetic Analysis

The electromagnetic performances of HSPMMs with different structures are presented and compared by FEM in this chapter [5,6]. As for material selection, NdFeB is selected as the PM material due to its high remanence and coercivity, and a silicon steel sheet is selected as the core material.

2.1. Main Dimensions of Motor

The stator inner diameter D and the motor active length L_{ef} which are called the main dimensions of the motor play an important role in motor design. The two main dimensions can be calculated by the following formulas:

$$D^2 L_{ef} = \frac{6.1}{\alpha'_P K_{nm} K_{dp} A B_\delta} \cdot \frac{P'}{n} \tag{1}$$

$$\lambda = \frac{L_{ef}}{\tau} \tag{2}$$

$$\tau = \frac{\pi D}{2P} \tag{3}$$

where P' is the apparent power, n is the motor speed, $\alpha_P{}'$ is the equivalent pole arc coefficient, K_{nm} is the air gap flux factor, K_{dp} is the winding factor, A is the line load, B_δ is the air gap flux density, λ is the main dimension ratio, τ is the pole distance, and P is the number of pole pairs.

The estimated values of each parameter in the above formula are shown in Table 1. Therefore, it can be roughly obtained that the D and the L_{ef} are 45 mm and 105 mm, respectively, which still needs to be further adjusted according to the subsequent analysis results.

Table 1. Calculation parameters of main dimensions of motor.

Parameters	Value	Parameters	Value
P' (kW)	27	A (A/m)	50,000
n (r/min)	30,000	B_δ (T)	0.7
$\alpha_P{}'$	0.7	λ	3
K_{nm}	1.11	P	2
K_{dp}	0.92		

Then, the air gap thickness and the outer diameter of the rotor can be set to 1.5 mm and 42 mm, which also need to be further optimized.

2.2. Number of Poles

The number of poles plays an important role in HSPMMs' electromagnetic performances. In order to limit the operating frequency of HSPMMs and suppress the losses caused by high-frequency current and high-frequency magnetic flux density, the number of poles of HSPMMs should better be set as two or four. The structural parameters and electromagnetic performances of two HSPMMs with two poles and four poles, respectively, are analyzed and compared in this paper. The two HSPMMs are designed with the same power (30 kW), same speed (30,000 r/min), and the same stator slots number (12).

The two HSPMMs' structural parameters are presented and compared in Table 2. It can be found the two poles motor has a lower frequency (500 Hz) than the four poles one (1000 Hz), which is beneficial to reduce stator iron loss and winding copper loss. However, the two poles motor has a larger size and lower power density than the four poles motor.

The two motors' back EMF and air gap magnetic flux density with FFT analysis results under no-load conditions are compared and shown in Figures 1 and 2, respectively.

Table 2. Structural parameters of 2 and 4 poles HSPMMs.

Parameters	2 Poles	4 Poles
Power (kW)	30	30
Speed (r/min)	30,000	30,000
Frequency (Hz)	500	1000
Stator outer diameter (mm)	118	103
Stator inner diameter (mm)	45	45
Slot number	12	12
Core length (mm)	130	105
Rotor outer diameter (mm)	42.2	42.2
Number of winding turns	7	8
Winding pitch	5	2

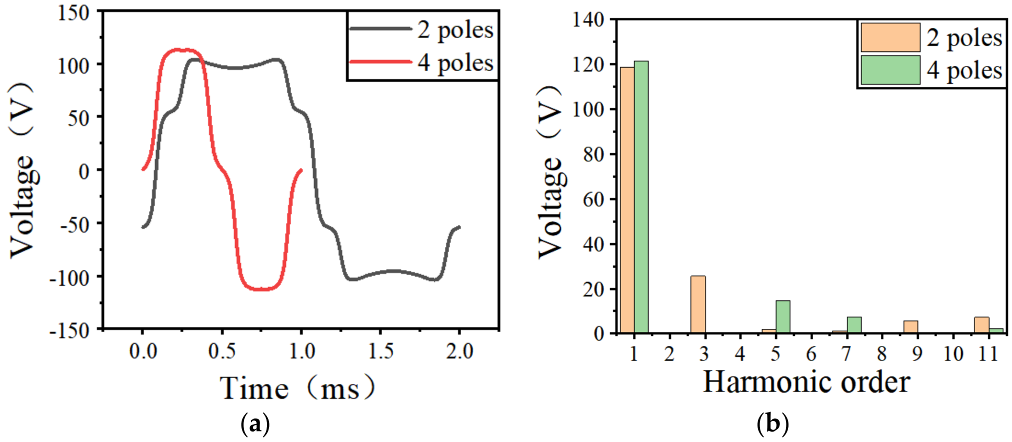

Figure 1. Waveforms and FFT analysis results of back EMF for 2 poles and 4 poles HSPMMs. (**a**) Waveforms; (**b**) FFT analysis results.

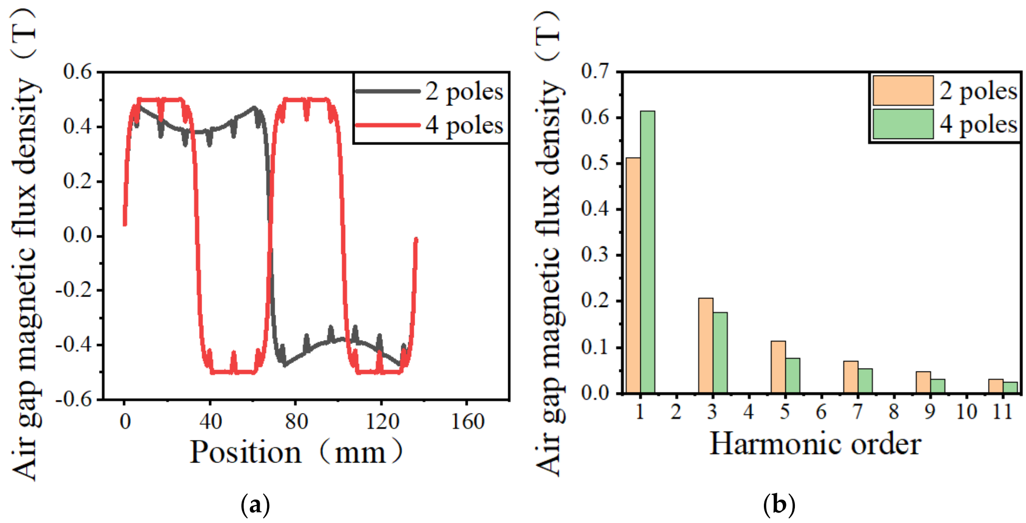

Figure 2. Waveforms and FFT analysis results of air gap magnetic flux density for 2 poles and 4 poles HSPMMs. (**a**) Waveforms; (**b**) FFT analysis results.

Figure 1 shows the two motors' back EMF waveforms with FFT analysis results. It can be found that the four poles motor has a larger fundamental component, the fifth harmonic component, and the seventh harmonic component, while other harmonic components are smaller than the two poles motor, especially the third harmonic component. In general, the back EMF of the four poles motor has lower harmonics, and the waveform of which is closer to the sine wave.

The two motors' air gap magnetic flux density waveforms with FFT analysis results are presented and compared in Figure 2. Each harmonic component of the air gap magnetic flux density of the four poles motor is lower than the two poles motor except for the fundamental component, indicating the four poles structure has better performance in reducing harmonics. Additionally, adopting the four poles structure for HSPMMs can also improve the utilization of PMs due to their higher fundamental component of air gap magnetic flux density.

The two motors' performances under full-load condition are also compared in this paper and shown in Figure 3 and Table 3. Due to the lower frequency, the two poles HSPMM has lower stator iron loss and winding copper loss than the four poles. Although the four poles HSPMM has lower eddy current loss and wind friction loss because of their smaller size and lower harmonics, the efficiency of the two poles HSPMM is still higher than the four poles HSPMM. Additionally, it can be found from Figure 3b and Table 3 that the two motors have the same average torque under full-load conditions, while the four poles motor has a larger torque ripple (13.84%) than the two poles (5.32%).

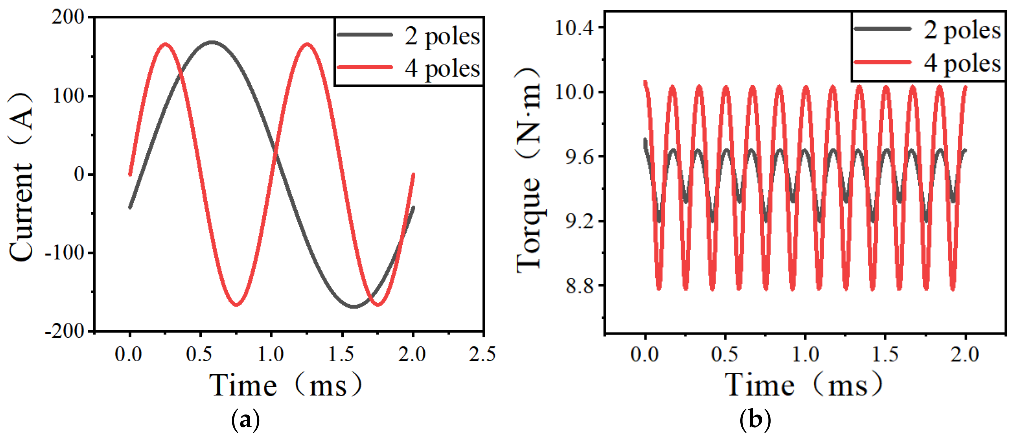

Figure 3. The comparisons of current and torque waveforms of the HSPMM under full-load conditions. (**a**) Current waveforms; (**b**) torque waveforms.

Table 3. Performances of 2 and 4 poles HSPMMs under full-load condition.

Parameters	2 Poles	4 Poles
RMS current (A)	117.10	117.28
Torque (N·m)	9.48	9.49
Torque ripple (%)	5.32	13.84
Stator iron loss (W)	321.43	558.68
Winding copper loss (W)	257.22	264.09
Rotor eddy current loss (W)	218.19	210.48
Wind friction loss (W)	72.53	58.58
Efficiency (%)	97.10	96.36

Finally, this paper chooses to adopt the four poles structure due to its lower harmonics, smaller size, higher power density, and lower rotor eddy current loss.

2.3. Number of Slots

As shown in Figure 4, there are three normally used stator structures of HSPMMs including slotless structure, less slot structure, and multi-slot structure. Considering the advantages of higher air-gap flux density, higher utilization of PMs, and lower harmonic amplitude, there is no doubt that the multi-slot structure has been the first choice in the design of HSPMM.

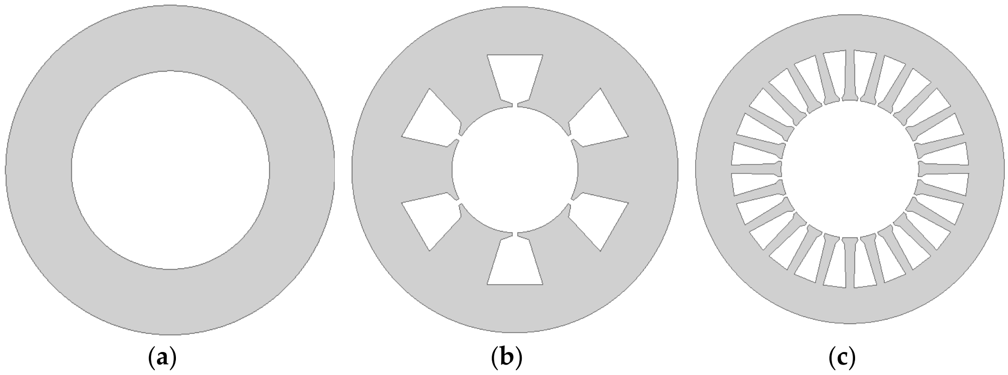

Figure 4. Stator structures of HSPMMs. (**a**) Slotless structure; (**b**) less slot structure; (**c**) multi slot structure.

In this paper, 3 HSPMMs with 12 slots, 18 slots, and 24 slots, respectively, are designed and compared to figure out the influence of the number of slots on HSPMMs. The three HSPMMs are designed with the same power, speed, frequency, number of poles, and size for a fair comparison.

Figure 5 shows the three HSPMMs' back EMF waveforms with FFT analysis results. It can be found that the 24 slots HSPMM has the largest fundamental component. Except for the third harmonic component, the other order harmonic components of the 24 slots HSPMM are lower than other motors, indicating that the multi-slot structure can help reduce harmonic components of back EMF.

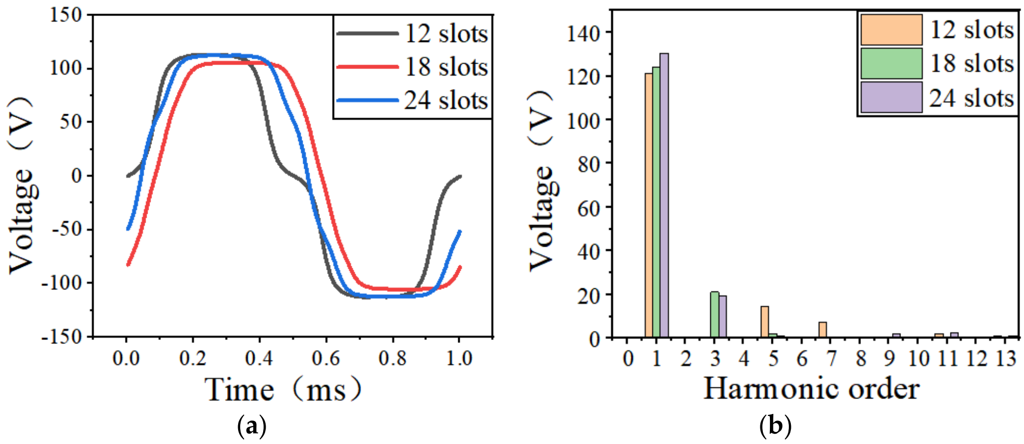

Figure 5. Waveforms and FFT analysis results of back EMF for 12 slots, 18 slots, and 24 slots HSPMMs. (**a**) Waveforms; (**b**) FFT analysis results.

The three HSPMMs' air gap magnetic flux density waveforms with FFT analysis under no-load conditions are presented in Figure 6. Due to the same rotor structure, the air gap magnetic flux density waveforms and FFT analysis results of the three motors are very similar to each other.

The performances of the three HSPMMs under full-load conditions are also compared and presented in Table 4. With the increase in the number of slots, the RMS current and torque ripple of HSPMMs is decreasing gradually. The three motors have nearly equal stator iron loss and wind friction loss since they have the same frequency and rotor size. The 18 slots motor has the lowest winding copper loss, though the RMS current of which is larger than the 24 slot one. The eddy current loss of 24 slots motor is much lower than other motors, which further proves that increasing the number of slots has good performance in the reduction of the harmonic components and the eddy current loss of HSPMMs.

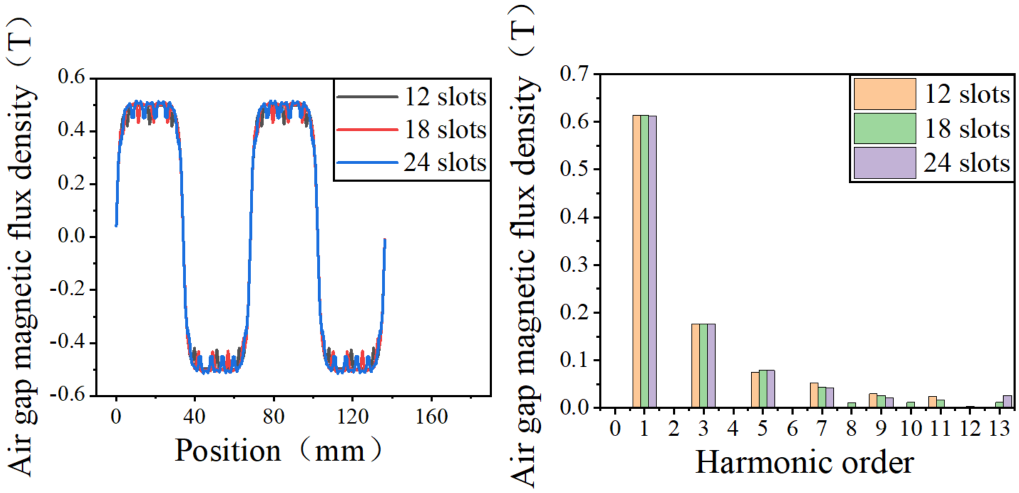

(**a**) (**b**)

Figure 6. Waveforms and FFT analysis results of air gap magnetic flux density for 12 slots, 18 slots, and 24 slots HSPMMs. (**a**) Waveforms; (**b**) FFT analysis results.

Table 4. Performances of 12 slots, 18 slots and 24 slots HSPMMs under full-load condition.

Parameters	12 Slots	18 Slots	24 Slots
RMS current (A)	117.28	114.61	108.59
Torque (N·m)	9.49	9.54	9.54
Torque ripple (%)	13.84	5.05	2.95
Stator iron loss (W)	558.68	554.87	558.81
Winding copper loss (W)	264.09	225.73	244.81
Rotor eddy current loss (W)	210.48	47.15	21.22
Wind friction loss (W)	58.58	58.58	58.58
Efficiency (%)	96.36	97.05	97.06

In summary, the 24 slots structure is a more reasonable choice for HSPMMs.

2.4. PM Magnetization Methods

The PM magnetization methods of HSPMMs mainly include radial magnetization, parallel magnetization, and Halbach magnetization, as shown in Figure 7. In order to figure out the influence of PM magnetization methods on the electromagnetic performances of HSPMMs, three HSPMMs with different PM magnetization methods are designed and compared in this paper. The three HSPMMs have the same power, speed, and frequency.

Figure 8 shows the magnetic flux density and line distributions of the three HSPMMs. According to Figure 8, It can be found that the color of the magnetic flux density cloud diagram in Figure 8c is generally lighter, indicating that the magnetic flux density of the motor with the Halbach magnetization method is lower than the other motors.

The three HSPMMs' back-EMF waveforms with FFT analysis results are presented in Figure 9. Then the RMS value of the total back EMF of the three motors calculated by FEM are 91.31 V (radial), 84.96 V (parallel), and 79.63 V (Halbach), respectively, indicating the HSPMM with the Halbach magnetization method has the smallest RMS value of total back EMF. Additionally, the back EMF waveform of the HSPMM with the Halbach magnetization method is closest to a sine wave due to its lower harmonic components.

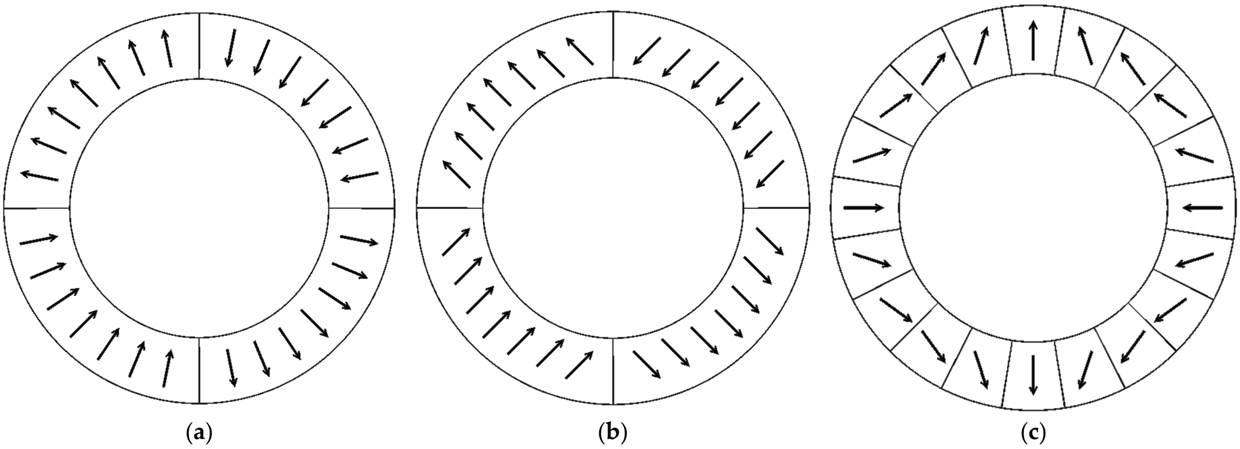

Figure 7. PM magnetization methods. (**a**) Radial magnetization; (**b**) parallel magnetization; (**c**) Halbach magnetization.

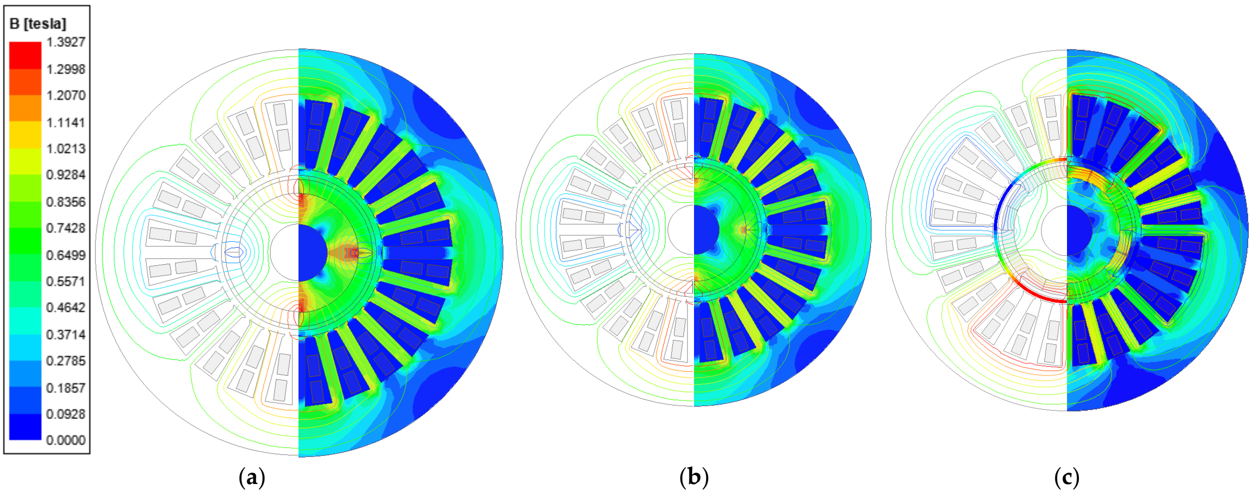

Figure 8. Magnetic flux density and lines distributions of HSPMMs with different magnetization methods under no-load condition. (**a**) Radial magnetization; (**b**) parallel magnetization; (**c**) Halbach magnetization.

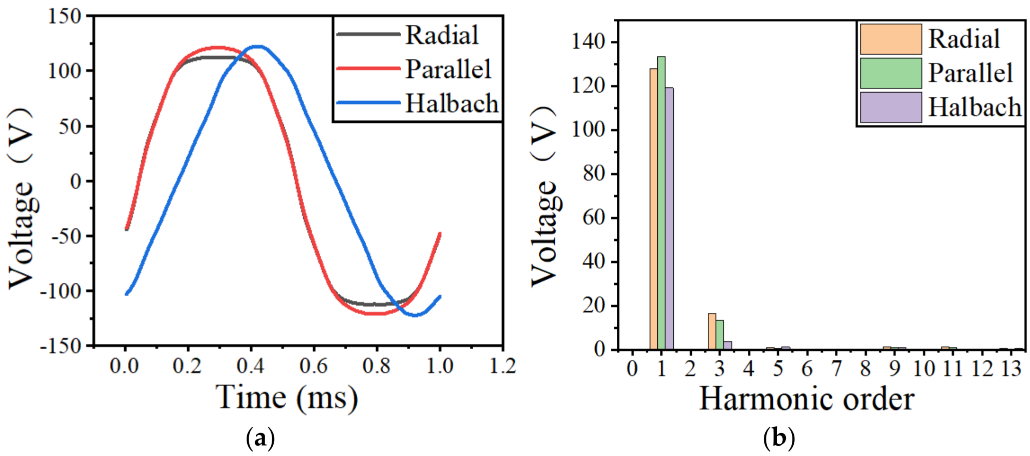

Figure 9. Waveforms and FFT analysis results of back EMF for HSPMMs with different magnetization methods. (**a**) Waveforms; (**b**) FFT analysis results.

The air gap magnetic flux density waveforms with FFT analysis results for the three HSPMMs are presented in Figure 10. It is learned that each harmonic component of air gap magnetic flux of the HSPMM with the Halbach magnetization method is lower than other motors except for the fifth harmonic component.

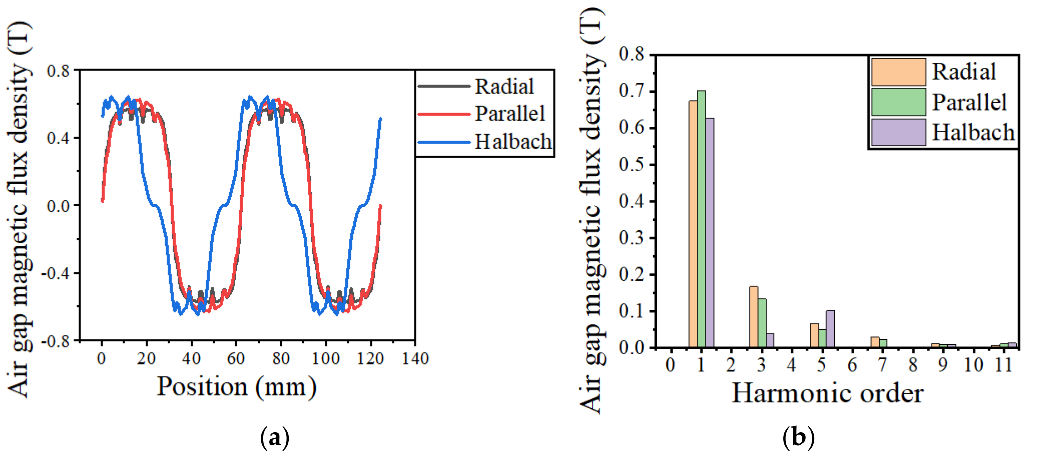

Figure 10. Waveforms and FFT analysis results of air gap magnetic flux density for HSPMMs with different magnetization methods. (**a**) Waveforms; (**b**) FFT analysis results.

The three HSPMMs' performances under full-load conditions are presented in Table 5. It can be learned that the HSPMM with PM parallel magnetized has the lowest current, the lowest torque ripple, the lowest rotor eddy current loss, and the highest efficiency.

Table 5. Performances of the three HSPMMs with different PM magnetization methods under full-load condition.

Parameters	Radial	Parallel	Halbach
RMS current (A)	110.89	106.15	119.02
Torque (N·m)	9.55	9.56	9.55
Torque ripple (%)	2.07	1.42	1.99
Stator iron loss (W)	511.09	478.63	437.87
Winding copper loss (W)	303.32	273.81	378.37
Rotor eddy current loss (W)	11.84	10.23	11.37
Wind friction loss (W)	33.16	33.16	33.16
Efficiency (%)	97.22	97.42	97.21

2.5. Final Electromagnetic Design Scheme

Based on the previous analysis, the electromagnetic design scheme of a 30 kW, 30,000 r/min HSPMM is finally completed in this paper. Figure 11 shows the current and torque waveforms of the HSPMM under full-load conditions, and the designed motor's structure and electromagnetic parameters are presented in detail in Table 6.

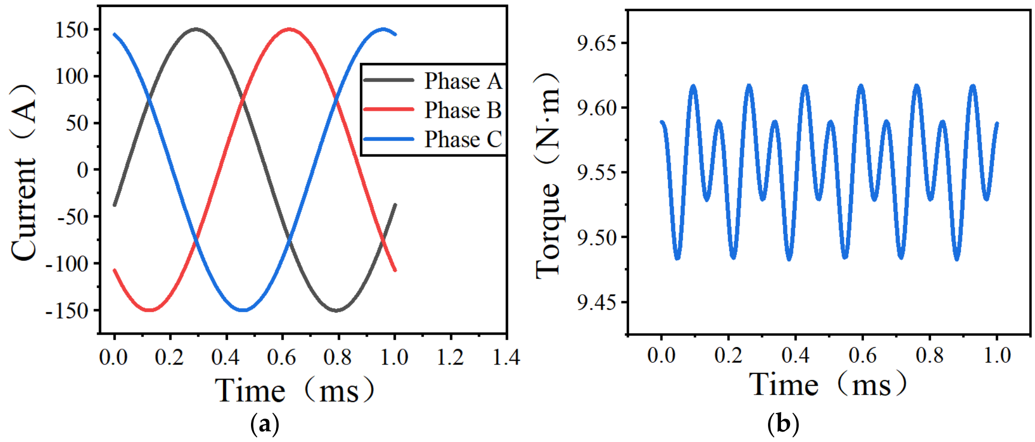

Figure 11. The current and torque waveforms of the HSPMM under full-load conditions. (**a**) Current waveform; (**b**) torque waveform.

Table 6. Structure and electromagnetic parameters of the 30 kW, 30,000 r/min HSPMM.

Parameters	Value	Parameters	Value
Power (kW)	30	Pole number	4
Speed (r/min)	30000	Slot number	24
Frequency (Hz)	1000	Stator outer diameter (mm)	100
RMS current (A)	106.15	Stator inner diameter (mm)	41
Torque (N·m)	9.56	Core length (mm)	103
Torque ripple (%)	1.42	Air gap thickness (mm)	1.5
Stator iron loss (W)	478.63	Rotor outer diameter (mm)	38
Winding copper loss (W)	273.81	Sleeve thickness (mm)	1
Rotor eddy current loss (W)	10.23	PM material	NdFeB
Wind friction loss (W)	33.16	PM thickness (mm)	3.4
Efficiency (%)	97.42	Magnetization direction	Parallel

3. Thermal Analysis

HSPMMs have limited heat dissipation capability due to their compact size and high loss density so a reasonable cooling system design is particularly necessary for HSPMMs. In this paper, CFD is selected to provide the thermal analysis for HSPMMs and study the cooling effects of different water-cooling methods [7,8].

3.1. Cooling Channel Structure

The structure of the three cooling channels is presented in Figure 12. Then, the comparative analysis of the thermal performances of HSPMMs with different cooling channel structures is performed in this paper. The three cooling channels are designed with the same inner surface area (13,229 mm^2), thickness (3 mm), and volume (40,774 mm^3) for comparison.

The calculation results of the heat transfer coefficient for the three HSPMMs are presented in Figure 13. It can be found the heat transfer coefficient of the spiral structure channel is higher than the other structures, indicating the spiral structure channel has better performance in heat dissipation. Therefore, as shown in Table 7, the maximum temperature of each component of the HSPMM with a spiral structure channel is the lowest of the three HSPMMs due to its higher heat transfer coefficient.

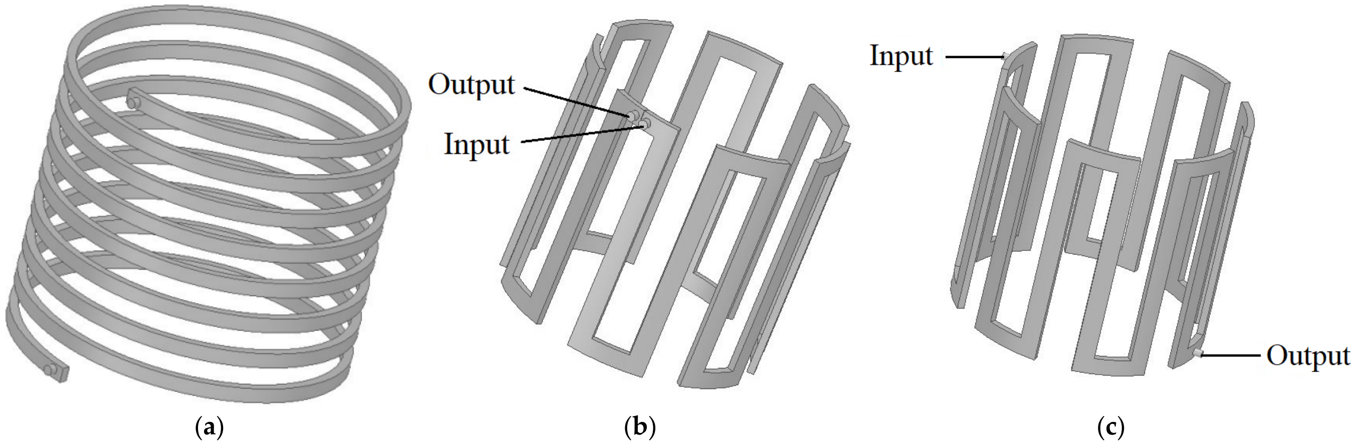

Figure 12. Cooling channel structures. (**a**) Spiral structure; (**b**) axial structure 1; (**c**) axial structure 2.

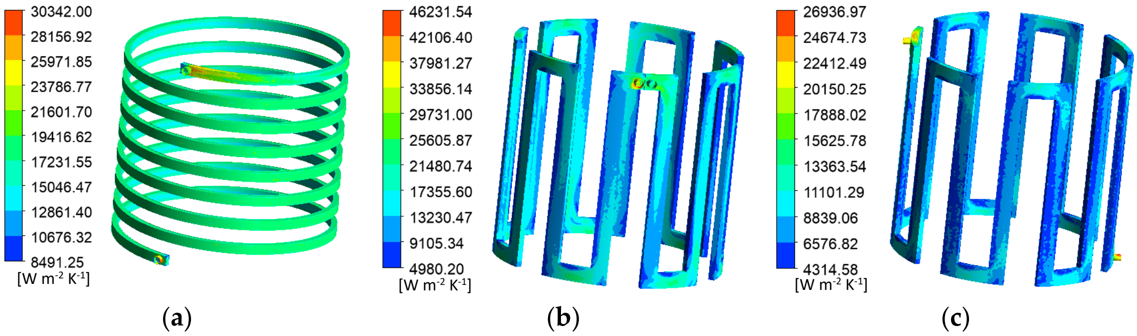

Figure 13. Heat transfer coefficient distribution of the three cooling channel structures. (**a**) Spiral structure; (**b**) axial structure 1; (**c**) axial structure 2.

Table 7. The maximum temperature of each part of motors with different cooling channel structures.

Parameters	Spiral	Axial 1	Axial 2
Cooling water (°C)	36.49	38.67	44.53
Stator core (°C)	66.08	66.63	68.80
Stator winding (°C)	69.96	70.84	73.99
Sleeve (°C)	124.89	125.01	131.91
PM (°C)	124.81	124.92	131.79

Figure 14 shows the pressure distribution of the three cooling channel structures. The axial channel 1 has the largest inlet pressure due to its larger channel angle and flow resistance. Correspondingly, the spiral channel has a smaller channel angle and flow resistance which contribute to its lower inlet pressure. In axial channel 2, the cooling water flows along two paths on both sides of the channel so that the actual flow distance is only half of the spiral channel and the axial channel 1. Therefore, the inlet pressure of the axial channel 2 is lower than other channels though it has a larger channel angle and flow resistance, too.

3.2. Number of Cooling Channel Turns

Considering the spiral cooling channel has a better cooling effect than other channel Structures, this paper provides further analysis of the number of spiral cooling channel turns.

The thermal analysis results of HSPMMs with a different number of cooling channel turns are shown in Figure 15. It can be found that with the rise of the number of cooling channel turns, the maximum temperature of cooling water and motor gradually reduced so that increasing the number of cooling channel turns is helpful to enhance the cooling effect.

However, when the number of channel turns is larger than eight, each motor component's maximum temperature hardly changed anymore, and even the cooling water maximum temperature rose slightly. Meanwhile, the eight-turn cooling channel has the largest heat transfer coefficient. Therefore, the number of cooling channel turns should be designed more reasonably with the considerations of both cooling effect and manufacturing difficulty.

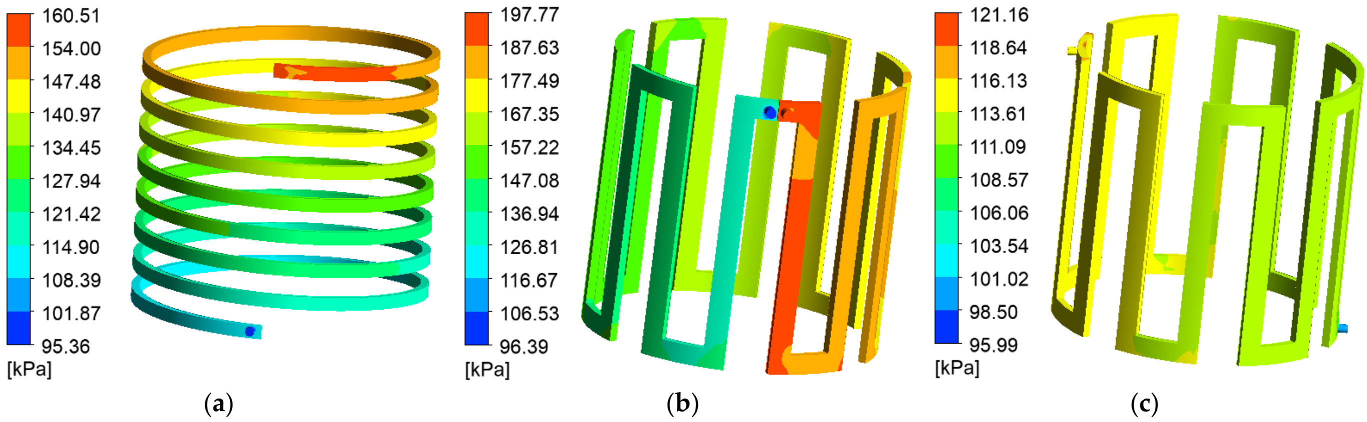

Figure 14. Pressure distribution of the three cooling channel structures. (**a**) Spiral structure; (**b**) axial structure 1; (**c**) axial structure 2.

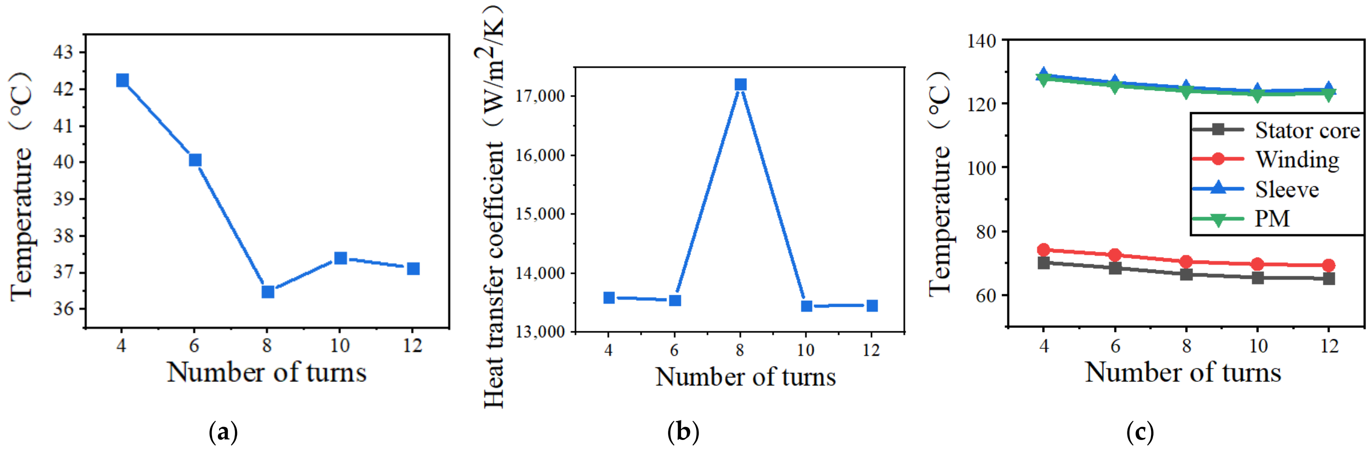

Figure 15. Thermal analysis results of HSPMMs with different number of cooling channel turns. (**a**) Cooling water maximum temperature; (**b**) Heat transfer coefficient; (**c**) Motor maximum temperature.

3.3. Cooling Water Flow Rate

The flow rate of cooling water also plays an important role in motor heat dissipation. Figure 16 shows the thermal analysis results of an HSPMM at different cooling water flow rates. It is learned that with the rise of the cooling water flow rate, the maximum temperature of the cooling water and the motor gradually decreased while the heat transfer coefficient of the cooling channel increased, indicating that increasing the cooling water flow rate can effectively enhance the cooling effect. However, when the flow rate is up to 3 m/s, the maximum temperature of the motor and the cooling water changes more slowly, indicating that continuing to increase the flow rate has few influences on the cooling effect, though the heat transfer coefficient still keeps increasing. Additionally, a high flow rate will also lead to an increase in inlet pressure and water pump power consumption.

Therefore, it is more reasonable to set the cooling water flow rate to 3 m/s.

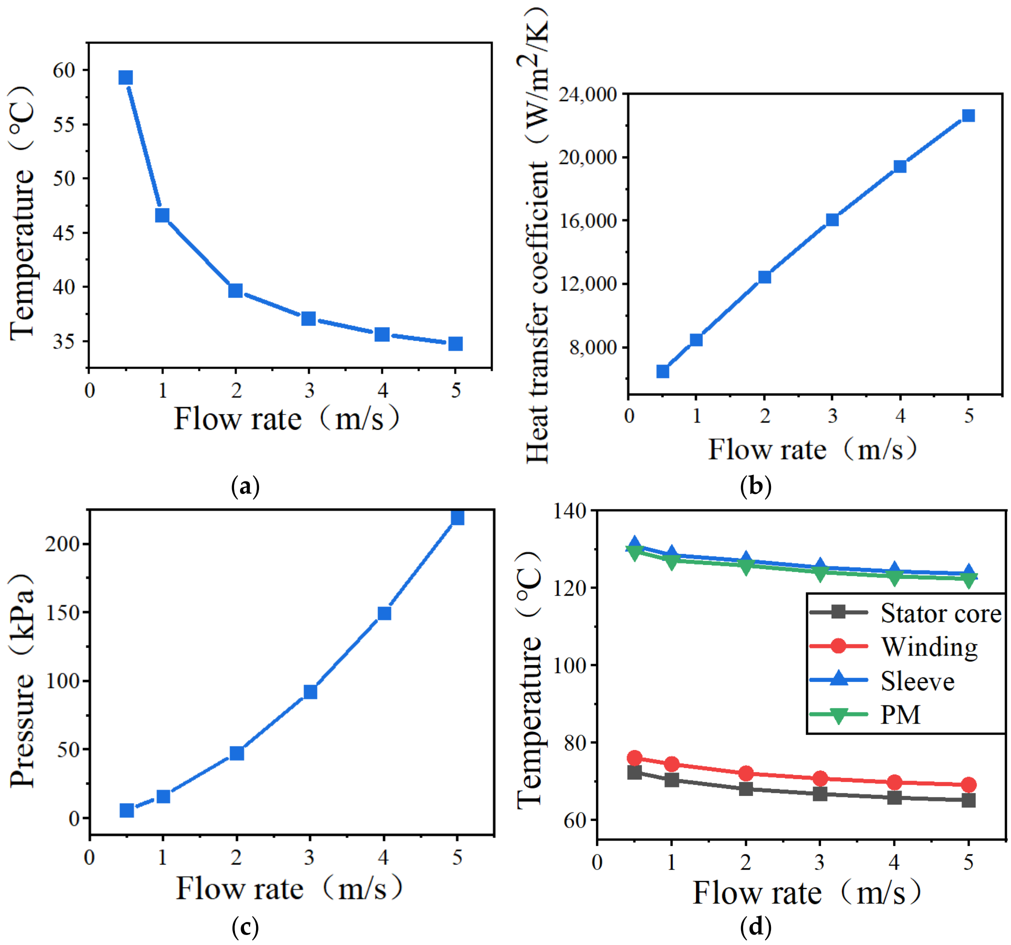

Figure 16. Thermal analysis results of HSPMMs at different cooling water flow rates. (**a**) Cooling water maximum temperature; (**b**) heat transfer coefficient; (**c**) inlet pressure; (**d**) motor maximum temperature.

3.4. Temperature Calculation Result

Finally, an eight turns spiral water channel is selected to protect the designed motor from overheating. The water flow rate is set as 3 m/s. The motor's temperature distribution calculated by CFD is shown in Figure 17. It can be found that the maximum temperature of the PM is 81.74 °C, which is much lower than the NdFeB's maximum permitted working temperature (180 °C), indicating the HSPMM designed in this paper has lower rotor loss density and the designed cooling method has better heat dissipation effect.

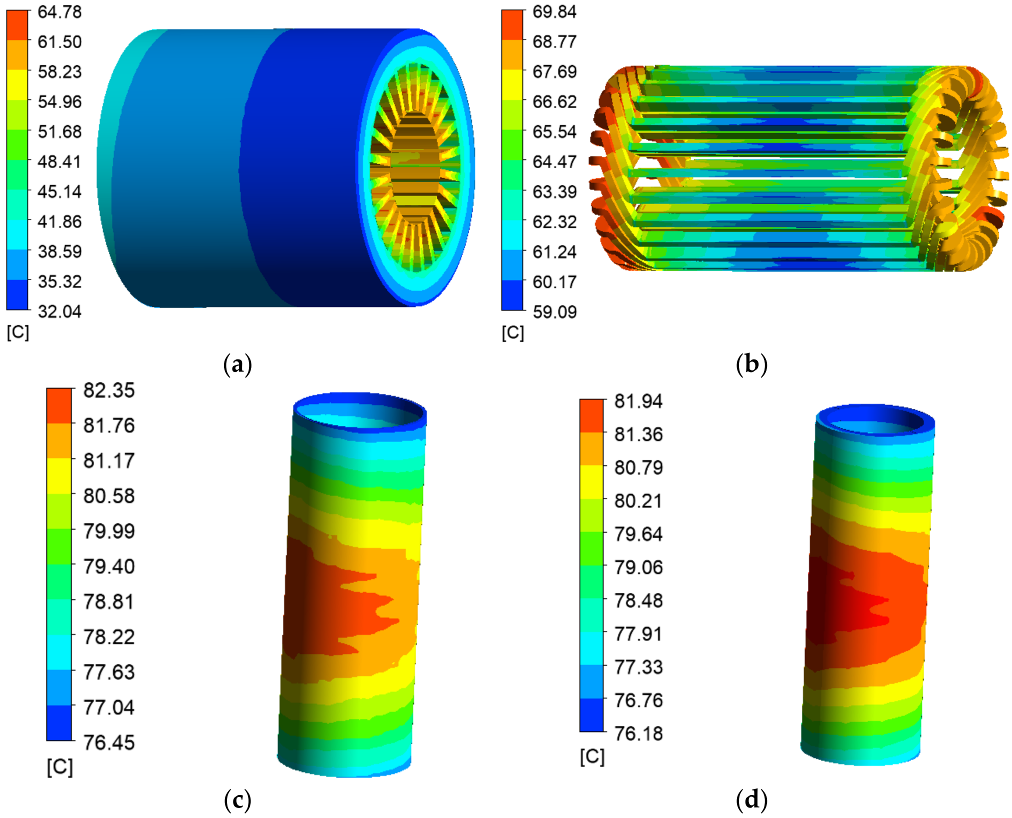

Figure 17. Temperature distribution of the designed motor. (**a**) Stator; (**b**) winding; (**c**) sleeve; (**d**) PM.

4. Stress Analysis

This paper provides the stress analysis for the sleeve–PM–core–shaft structure rotor of HSPMM by both the analytic method and FEM method [9]. The stainless sleeve with interference is adopted to protect the PM due to its better heat dissipation and strength. The stress analysis model of that structure rotor is shown in Figure 18.

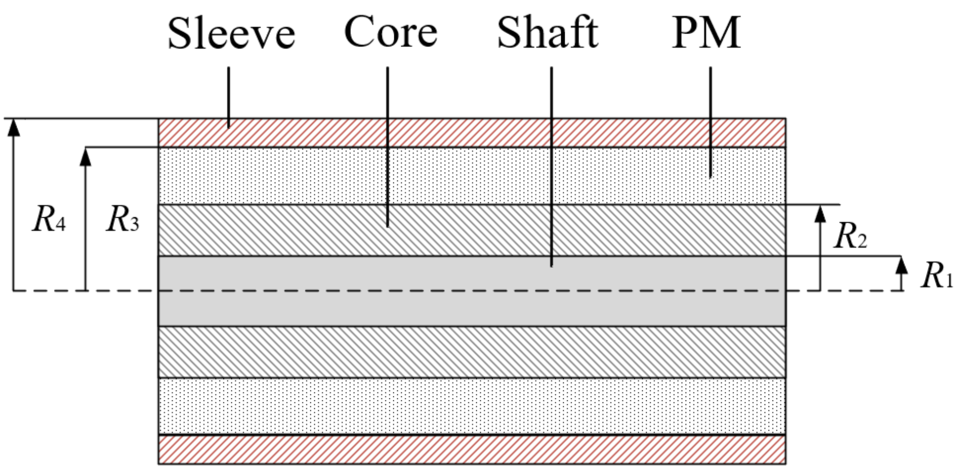

Figure 18. Stress analysis model of the sleeve–PM–core–shaft structure rotor.

4.1. Analytic Method

The sleeve–PM–core–shaft structure rotor can be equivalent to four thick-walled cylinder models, and the adjacent models are closely fitted. The pressure on the inner and outer surfaces of each cylinder model can be considered uniformly distributed. All the relevant properties of the cylinder model materials are isotropic. Then, a single-cylinder model is analyzed at first.

According to the material mechanics theory and geometric relationship, the strain-displacement relationship of the cylinder model can be described by [10]:

$$\begin{cases} \varepsilon_{\mathrm{r}} = \frac{du}{dr} \\ \varepsilon_{\theta} = \frac{du}{dr} \end{cases} \tag{4}$$

where the ε_{r} is the cylinder radial strain, ε_{θ} is the cylinder tangential strain, u is the cylinder displacement.

According to the Hooke's law, the stress–strain relationship can be described by:

$$\begin{cases} \varepsilon_{\mathrm{r}} = \frac{\sigma_{\mathrm{r}} - \mu\sigma_{\theta}}{E} + \alpha\Delta T \\ \varepsilon_{\theta} = \frac{\sigma_{\theta} - \mu\sigma_{\mathrm{r}}}{E} + \alpha\Delta T \end{cases} \tag{5}$$

where the σ_{r} is the cylinder radial stress, σ_{θ} is the cylinder tangential stress, μ is the cylinder Poisson's ratio, E is the cylinder young's modulus, α is the cylinder thermal expansion coefficient, ΔT is the cylinder temperature rise.

The force balance equation of the cylinder in the rotating condition can be described by:

$$\frac{d\sigma_{\mathrm{r}}}{dr} + \frac{\sigma_{\mathrm{r}} - \sigma_{\theta}}{r} + \rho\omega^2 r = 0 \tag{6}$$

where the ρ is the cylinder density, ω is the cylinder rotational angular velocity.

According to Equations (4)–(6), the u, σ_{r}, and σ_{θ} of a single-cylinder model can be obtained as follows:

$$u = Mr + \frac{N}{r} + \frac{(\mu^2 - 1)\rho\omega^2 r^3}{8E} \tag{7}$$

$$\begin{cases} \sigma_{\mathrm{r}} = \frac{ME}{1-\mu} - \frac{NE}{(1+\mu)r^2} - \frac{(3+\mu)\rho\omega^2 r^2}{8} - \frac{E\alpha\Delta T}{1-\mu} \\ \sigma_{\theta} = \frac{ME}{1-\mu} + \frac{NE}{(1+\mu)r^2} - \frac{(1+3\mu)\rho\omega^2 r^2}{8} - \frac{E\alpha\Delta T}{1-\mu} \end{cases} \tag{8}$$

where the M and N is the calculation coefficient.

According to Equations (7) and (8), the calculation equations for the displacement and stress of the sleeve–PM–core–shaft structure rotor can be obtained as follows:

$$u_{\mathrm{a}} = M_{\mathrm{a}} r + \frac{N_{\mathrm{a}}}{r} + \frac{({\mu_{\mathrm{a}}}^2 - 1)\rho_{\mathrm{a}}\omega^2 r^3}{8E_{\mathrm{a}}} \tag{9}$$

$$\begin{cases} \sigma_{\mathrm{ra}} = \frac{M_{\mathrm{a}}E_{\mathrm{a}}}{1-\mu_{\mathrm{a}}} - \frac{N_{\mathrm{a}}E_{\mathrm{a}}}{(1+\mu_{\mathrm{a}})r^2} - \frac{(3+\mu_{\mathrm{a}})\rho_{\mathrm{a}}\omega^2 r^2}{8} - \frac{E_{\mathrm{a}}\alpha_{\mathrm{a}}\Delta T_{\mathrm{a}}}{1-\mu_{\mathrm{a}}} \\ \sigma_{\theta\mathrm{a}} = \frac{M_{\mathrm{a}}E_{\mathrm{a}}}{1-\mu_{\mathrm{a}}} + \frac{N_{\mathrm{a}}E_{\mathrm{a}}}{(1+\mu_{\mathrm{a}})r^2} - \frac{(1+3\mu_{\mathrm{a}})\rho_{\mathrm{a}}\omega^2 r^2}{8} - \frac{E_{\mathrm{a}}\alpha_{\mathrm{a}}\Delta T_{\mathrm{a}}}{1-\mu_{\mathrm{a}}} \end{cases} \tag{10}$$

where the a = 1, 2, 3, and 4, corresponding to the equations of the shaft, core, PM, and sleeve, respectively. Considering that the displacement at the center of the shaft is 0, so that the N_1 is 0.

The stress and displacement boundary conditions for the sleeve–PM–core–shaft structure rotor are as follows:

$$\begin{cases} u_1(r = R_1) = u_2(r = R_1) \\ u_2(r = R_2) = u_3(r = R_2) \\ u_4(r = R_3) - u_3(r = R_3) = \delta \\ \sigma_{\mathrm{r}1}(r = R_1) = \sigma_{\mathrm{r}2}(r = R_1) \\ \sigma_{\mathrm{r}2}(r = R_2) = \sigma_{\mathrm{r}3}(r = R_2) \\ \sigma_{\mathrm{r}3}(r = R_3) = \sigma_{\mathrm{r}4}(r = R_3) \\ \sigma_{\mathrm{r}4}(r = R_4) = 0 \end{cases} \tag{11}$$

where the δ is the interference between sleeve and PM.

Finally, the calculation coefficients in Equations (9) and (10) and the complete stress analytical equations of the sleeve–PM–core–shaft structure rotor can be obtained by Equation (11).

4.2. FEM Verification

In order to verify the accuracy of the proposed analytic method, this paper adopts both the analytic method and FEM to calculate the stress distributions of a sleeve–PM–core–shaft structure rotor for comparison.

The stress distributions calculated by the two methods are shown in Figure 19. It can be found that there are certain acceptable errors in both the PM radial stress and tangential stress calculated by the two methods. Meanwhile, the analytical result of sleeve equivalent stress agrees well with the FEM one and the calculation error rate between the two methods is only 0.36%. Therefore, it can be considered that the analytic method provided by this paper can accurately calculate the stress distribution of the sleeve–PM–core–shaft structure rotor.

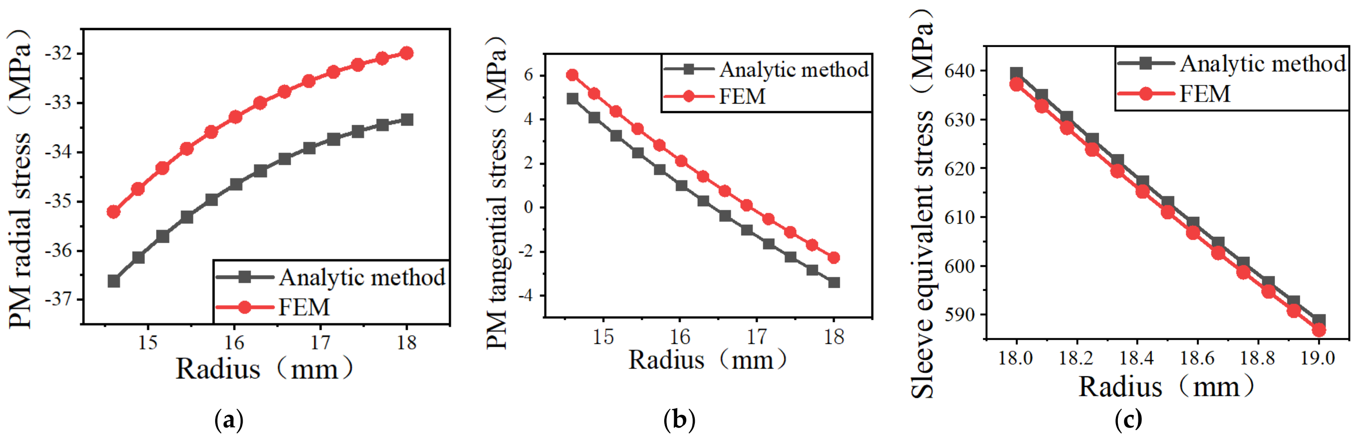

Figure 19. Stress distribution of the sleeve–PM–core–shaft structure rotor. (**a**) PM radial stress; (**b**) PM tangential stress; (**c**) sleeve equivalent stress.

4.3. Influencing Factors

Both the sleeve thickness and the interference have significant effects on the rotor stress distribution. The maximum stress of the rotor variations with sleeve thicknesses and interferences is presented in Figure 20. It can be found that increasing the interference is more conducive to reducing the maximum tensile stress of the PM in both radial and tangential directions, while the maximum equivalent stress of the sleeve will increase accordingly. Additionally, the larger thickness of the sleeve also has the advantage of reducing the tensile stress of the PM, but it has little effect on the reduction of sleeve equivalent stress.

4.4. Final Rotor Mechanical Protection Scheme

According to the above analysis, this paper finally adopts a stainless steel sleeve of 1 mm to mechanically protect the rotor of the HSPMM, and the interference between the sleeve and the PM is set to 0.05 mm. Then, the designed motor's rotor stress distribution is calculated by FEM and the result of which is shown in Figure 21. It is learned that the PM bears compressive stress in both radial and tangential directions, while the PM material has a strong tolerance to compressive stress. Meanwhile, the maximum equivalent stress of the sleeve is 537.19 MPa, which is lower than the permitted value of stainless steel (1100 MPa). Therefore, the final rotor mechanical protection scheme designed in this paper is reliable.

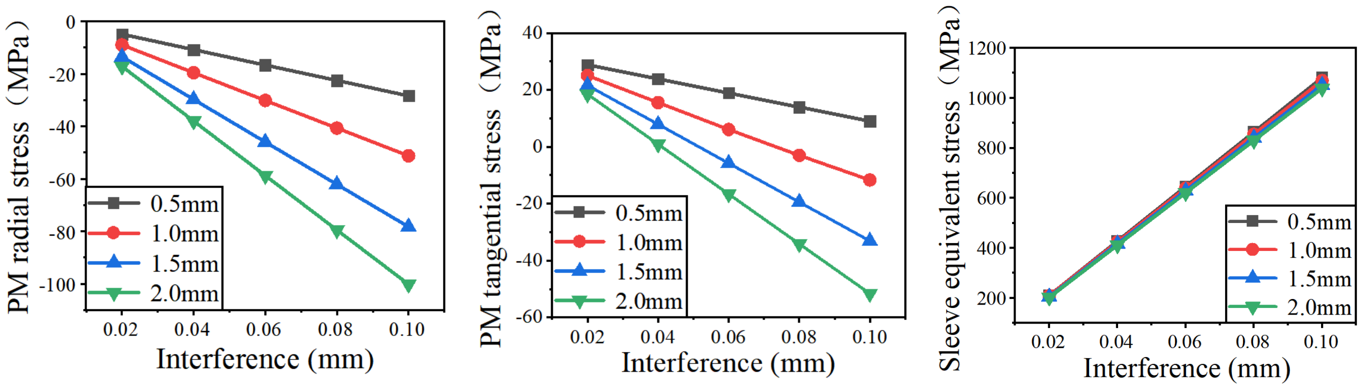

(**a**) (**b**) (**c**)

Figure 20. The maximum stress of the rotor variations with sleeve thickness and interference. (**a**) PM maximum radial stress; (**b**) PM maximum tangential stress; (**c**) sleeve maximum equivalent stress.

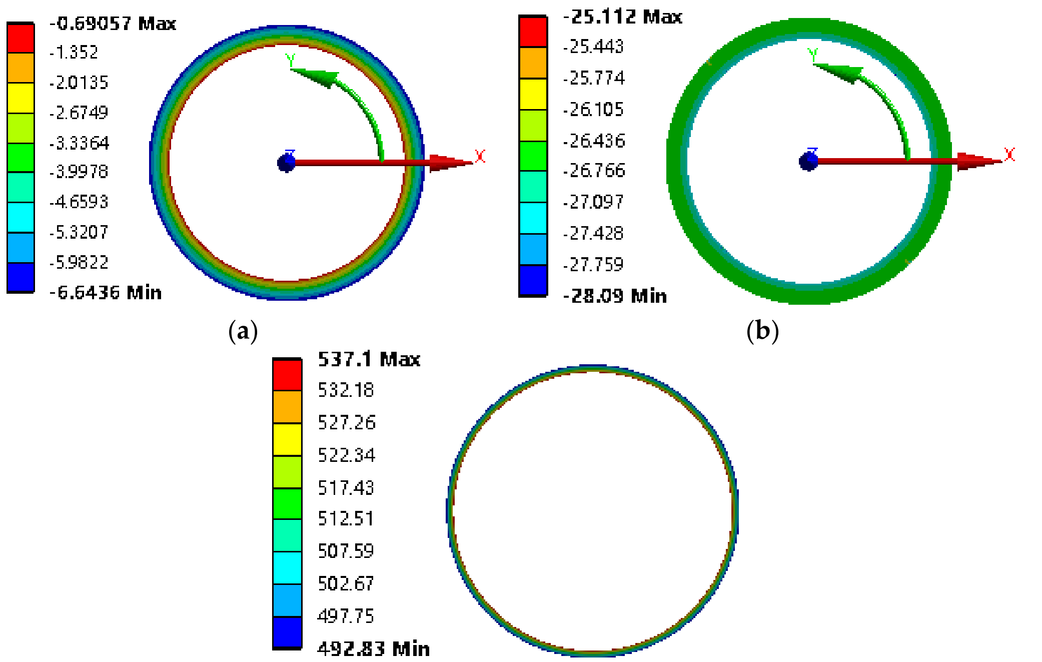

(**a**) (**b**) (**c**)

Figure 21. The designed motor's rotor stress distribution. (**a**) PM radial stress; (**b**) PM tangential stress; (**c**) sleeve equivalent stress.

5. Conclusions

This paper provides the design and analysis of a 30 kW, 30,000 r/min high-speed permanent magnet motor (HSPMM) for compressor application. Firstly, the effects of the number of poles, the number of slots, and the PM magnetization methods on the electromagnetic performance of the motor are studied. It is found the four poles, and twenty-four slots motor with PM parallel magnetized has better electromagnetic performance. Then, the CFD is adopted to provide thermal analysis for HSPMMs with different cooling channel structures and different channel turn numbers, and it is found the eight turns spiral water channel with a flow rate of 3 m/s is more beneficial for heat dissipation. The analytic method of the sleeve–PM–core–shaft structure rotor stress distribution is proposed in this paper. This paper provides a comparative analysis between the analytic method and the FEM of the rotor stress, proving the analytic method is reliable. Finally, the influencing factors of rotor stress distribution are analyzed in this paper. According to the analysis results, this paper adopts a stainless steel sleeve of 1 mm to mechanically protect the rotor of the HSPMM, and the interference between the sleeve and the PM is set to 0.05 mm. The rotor stress FEM calculation results of the designed motor show the fact that the rotor protection scheme adopted in this paper is reliable.

Author Contributions: Conceptualization, Z.Q. and Y.Z.; methodology, Z.Q. and Y.Z.; software, Y.Z., S.Y. and Z.X.; validation, Y.Z., S.Y. and Z.X.; formal analysis, Y.Z.; investigation, Z.Q. and Y.Z.; resources, Y.Z.; data curation, Z.Q.; writing—original draft preparation, Z.Q.; writing—review and editing, Z.Q. and Y.Z.; visualization, Z.Q. and Y.Z.; supervision, Y.Z.; project administration, Y.Z.; funding acquisition, Y.Z. All authors have read and agreed to the published version of the manuscript.

Funding: This research was funded by the Ministry of Science and Technology under the National Key R&D Program of China (Grant No. 2021YFE0108600). And this research is also funded by the National Natural Science Foundation of China under grant 52077121, and the National Natural Science Foundation of China Key International Cooperation project under grant 51920105011. This research is also funded by the Natural Science Foundation of Liaoning province under grant 2021-KF-24-01.

Institutional Review Board Statement: Not applicable.

Informed Consent Statement: Not applicable.

Data Availability Statement: Not applicable.

Conflicts of Interest: The authors declare no conflict of interest.

References

1. Gerada, D.; Mebarki, A.; Brown, N.L.; Gerada, C.; Cavagnino, A.; Boglietti, A. High-speed Electrical Machines: Technologies, Trends, and Developments. *IEEE Trans. Ind. Electron.* **2014**, *61*, 2946–2959. [CrossRef]
2. Bianchi, N.; Bolognani, S.; Luise, F. Potentials and Limits of High-Speed PM Motors. *IEEE Trans. Ind. Appl.* **2004**, *40*, 1570–1578. [CrossRef]
3. Li, S.; Li, Y.; Choi, W.; Sarlioglu, B. High-Speed Electric Machines: Challenges and Design Considerations. *IEEE Trans. Transp. Electrif.* **2016**, *2*, 2–13. [CrossRef]
4. Zhang, F.; Dai, R.; Liu, G.; Cui, T. Design of HSIPMM Based on Multi-physics Fields. *IET Electr. Power Appl.* **2018**, *12*, 1098–1103. [CrossRef]
5. Jing, L.; Tang, W.; Wang, T.; Ben, T.; Qu, R. Performance Analysis of Magnetically Geared Permanent Magnet Brushless Motor for Hybrid Electric Vehicles. *IEEE Trans. Transp. Electrif.* **2022**, *8*, 2874–2883. [CrossRef]
6. Jing, L.; Pan, Y.; Wang, T.; Qu, R.; Cheng, P.T. Transient Analysis and Verification of a Magnetic Gear Integrated Permanent Magnet Brushless Machine with Halbach Arrays. *IEEE J. Emerg. Sel. Top. Power Electron.* **2022**, *10*, 1881–1890. [CrossRef]
7. Dong, J.; Huang, Y.; Jin, L.; Lin, H.; Yang, H. Thermal Optimization of a High-Speed Permanent Magnet Motor. *IEEE Trans. Magn.* **2014**, *50*, 7018504. [CrossRef]
8. Tong, W.; Sun, R.; Zhang, C.; Wu, S.; Tang, R. Loss and Thermal Analysis of a High-Speed Surface-Mounted PMSM with Amorphous Metal Stator Core and Titanium Alloy Rotor Sleeve. *IEEE Trans. Magn.* **2019**, *55*, 8102104. [CrossRef]
9. Du, G.; Xu, W.; Zhu, J.; Huang, N. Rotor Stress Analysis for High-Speed Permanent Magnet Machines Considering Assembly Gap and Temperature Gradient. *IEEE Trans. Energy Convers.* **2019**, *34*, 2276–2285. [CrossRef]
10. Shen, J.; Qin, X.; Yao, L.; Wang, Y. Rotor Strength Analysis and Retaining Sleeve Design for High-speed PM Machines. *Proc. CSEE* **2022**, *42*, 2334–2346.